Journal of Materials Chemistry A

Exploring the Mobility of Cu in Bimetallic Nanocrystals to Promote Atomic-Scale Transformations under a Reactive Gas Environment

Journal:	*Journal of Materials Chemistry A*
Manuscript ID	TA-ART-01-2023-000458.R1
Article Type:	Paper
Date Submitted by the Author:	02-Apr-2023
Complete List of Authors:	Mathiesen, Jette; Technical University of Denmark, Department of Physics ; University of Copenhagen, Center for High Entropy Alloy Catalysis (CHEAC), Department of Chemistry Colding-Fagerholt, Sofie; Technical University of Denmark, Department of Physics; Technical University of Denmark, Center for Visualizing Catalytic Processes (VISION), Department of Physics Degn Jensen, Kim; University of Copenhagen, Chemistry Pedersen, Jack; University of Copenhagen, Center for High Entropy Alloy Catalysis (CHEAC), Department of Chemistry Vosch, Tom; University of Copenhagen, Department of Chemistry Rossmeisl, Jan; University of Copenhagen, Center for High Entropy Alloy Catalysis (CHEAC), Department of Chemistry helveg, stig; Technical University of Denmark, Department of Physics; Technical University of Denmark, Center for Visualizing Catalytic Processes (VISION), Department of Physics Jensen, Kirsten Marie; University of Copenhagen, Center for High Entropy Alloy Catalysis (CHEAC), Department of Chemistry, Dept. of Chemistry

ARTICLE

Exploring the Mobility of Cu in Bimetallic Nanocrystals to Promote Atomic-Scale Transformations under a Reactive Gas Environment

Received 00th January 20xx,
Accepted 00th January 20xx

DOI: 10.1039/x0xx00000x

Jette K. Mathiesen,*[a,c] Sofie Colding-Fagerholt,[b] Kim D. Jensen,[c] Jack K. Pedersen,[c] Tom Vosch,[a] Jan Rossmeisl,[c] Stig Helveg[b] and Kirsten M. Ø. Jensen*[c]

Bimetallic nanocrystals (NCs) often show improved catalytic activities compared to their monometallic counterparts, but to optimize the performance it is crucial to understand how they behave under actual reaction conditions, i.e. in gas environments. Here, we use powder X-ray diffraction (PXRD), total scattering (TS) with pair distribution function (PDF) analysis and *in situ* high-resolution transmission electron microscopy (HR-TEM) to provide new insights into the atomic-scale behaviour of NC catalysts under a reactive gas environment. By investigating Au, Cu, Pd, PdCu, AuPd and AuCu NCs, we observe that the properties of bimetallic NCs differ significantly from their monometallic counterparts. While metal oxide phases formed for monometallic Pd and Cu under O_2-exposure, bimetallic PdCu and AuCu NCs showed loss of metallic Cu in the crystalline phases present after exposure to O_2. However, upon introducing the bimetallic NCs to a reducing atmosphere, the Cu was found to reappear and reincorporate into a crystalline phase, forming the initial bimetallic structures. By combining TS, PDF analysis and *in situ* HR-TEM, we saw that Cu segregates to the NC surfaces or forms small CuO domains under O_2-exposure. Our results thus indicate that the Cu mobility promotes segregation and formation of CuO along with the formation of a monometallic phase, which ultimately changes the resulting active surface sites of the nanocatalyst. Understanding the dynamical structure-property relations of nanocatalysts is key to enable rational design of efficient and robust catalysts for controlled catalytic reactions.

Introduction

Bimetallic nanocrystals (NCs) have received much attention in recent years, *e.g.* for their use within heterogenous catalysis, since their catalytic properties often differ significantly from their monometallic counterparts.[1] For example, AuPd alloys have shown to be more efficient than monometallic Pd for the oxidation of alcohols towards carbonyl compounds by preventing the formation of Pd oxide, which due to its catalytical inertness rapidly lowers the activity of pure Pd catalysts.[2, 3]

The altered surface properties of bimetallic NCs have been proposed to arise from two primary effects denoted the *ligand* and *strain* effects.[4, 5] Ligand (or ensemble) effects refer to the changes in local chemisorption properties induced by the specific atomic arrangement at the active adsorption site.[6] Strain effects, on the other hand, describe changes in the electronic properties of the surface atoms resulting from the stretching or compression of the local atomic crystal structure.[7] The two effects can be difficult to distinguish from one another. The electron donation between atoms of varying electronegativity changes the electronic surface structure and thereby the surface-adsorbate interactions.[8, 9] As a result, these effects contribute considerably to the performance of bimetallic catalysts by impacting the properties of the active sites.[10] Design of new improved catalysts, with tuned properties towards specific adsorbate binding, thus relies on understanding how introducing new metallic species influences the atomic structure and the resulting active sites of the catalyst.

However, the nature of the active surface sites is not purely a result of the elemental composition of the NCs, as small catalytic bimetallic NCs are known to respond dynamically to their surroundings by restructuring, dissolving, oxidizing/reducing and sintering.[11-20] Small NCs have higher surface energies, which means that they are more prone to reconstruction.[21] Restructuring has also been attributed to the changing adsorbate-surface interactions under reaction conditions, where the differences in binding strength of an adsorbate and the different metals composing the bimetallic NC induce structural changes.[22-25] Thus, characterizing catalytic NCs

[a] *SurfaceCatlysis (SURFCAT), Department of Physics, Technical University of Denmark, DK-2800 Kgs. Lyngby, Denmark.*
[b] *Center for Visualizing Catalytic Processes (VISION), Department of Physics, Technical University of Denmark, DK-2800 Kgs. Lyngby, Denmark.*
[c] *Center for High Entropy Alloy Catalysis (CHEAC), Department of Chemistry, University of Copenhagen, Universitetsparken 5, 2100 Copenhagen, Denmark*
[d] *Department of Chemistry, University of Copenhagen, Universitetsparken 5, 2100 Copenhagen, Denmark*
Electronic Supplementary Information (ESI) available: [details of any supplementary information available should be included here]. See DOI: 10.1039/x0xx00000x

involves understanding their atomic and nanoscale structure before, during (*i.e. operando*) and after the applied pre-treatment or catalytic reaction conditions of interest have been met. Such characterization is required to establish a coherent and complete picture of the NCs' physical properties and stability. Employment of multiple techniques covering various length- and time scales is provisional for such elaborate understanding of the catalytical NCs' to dynamical structural responses. Previously, environmental restructuring in bimetallic NCs has been observed using ambient-pressure X-ray photoelectron spectroscopy (AP-XPS), Fourier-transform infrared spectroscopy (FTIR) and *in-* and *ex situ* transmission electron microscopy (TEM).[11] In a CoPd NC system, the combination of multiple techniques allowed for the observation of CO-induced restructuring. This was manifested by the formation of CoO species on the surface, which promoted CO oxidation in the system.[11] CO-induced structural reconstruction has also been observed *in situ* in Pt-containing mono- and multimetallic NCs using X-ray total scattering (TS) with subsequent pair distribution function (PDF) analysis.[26-28] From PDF analysis, structural changes in Pt, PtAu and PtAuNi systems were found to be limited to the NCs surface as either a change in the active site availability, gas-induced disorder or changes in the atomic packing during CO oxidation.[26-28] Important insights into CO-induced structural disorder on the surface of metallic NCs has furthermore been obtained by combining *in situ* PDF analysis and *in situ* diffuse reflection infrared Fourier transform spectroscopy (DRIFTS).[28] The combination of PDF and DRIFTS enabled investigation and identification of correlations between the NCs' structure and the chemical binding at the surface under reaction conditions. This offered insights into the catalyst's functionality and demonstrated the importance of applying different complementary techniques to obtain the full picture of promising nanocatalysts.

Using multiple characterization techniques, we herein show that the exposure to different single reactant gas environments can be used to stabilize different structures of mono- and bimetallic NCs, highlighting a significant divergence from the pristine structure. From a detailed atomic level evaluation using powder X-ray diffraction (PXRD), X-ray TS and *in situ* high-resolution TEM (HR-TEM), we observe distinct bulk and surface reconstruction of the NCs. More importantly, it is found that the structural response of bimetallic NCs cannot simply be considered as a linear interpolation of the effects observed for the monometallic species. Instead, it shows that alloying directly affects the restructuring processes, which is evident by the formation of new structures. Although different reactive gases may be competitively adsorbed on a metal surface under real reaction conditions, we here provide insights into how the individual gasses induce restructuring for a preliminary understanding of how the metals will behave under actual conditions. In addition, these simple, single gas experiments might also enable the ability to deconvolute the effect of individual gasses on the restructuring behaviour under real reaction conditions to assign the adsorption phenomena that is responsible for the observed restructuring. Consequently, these findings highlight the strength of combining multiple *in situ* and *ex situ* characterization tools to provide a first-hand impression of what can be expected under commonly used pre-treatments or catalytic reaction conditions of similar oxidation and reduction potentials. Providing such insights are crucial to establish structure-property relations of the nanocatalysts as a stepping stone for the future development of highly active catalysts to fuel our future.

Experimental

Chemicals. Oleylamine (70%, OLA), oleic acid (90%, OA), trioctylphosphine (97%, TOP), copper (II) acetate (98%, $Cu(ac)_2$), palladium (II) bromide (99%, $PdBr_2$), palladium (II) hexafluoroacetyl acetonate ($Pd(hfacac)_2$), were purchased from Sigma Aldrich. Gold (III) acetate ($Au(ac)_3$) was purchased from Alfa Aesar. All reagents were used as received.

Synthesis of bimetallic NCS

The bimetallic NCs were synthesized with equimolar metal constituents according to a previously reported synthesis procedure.[29, 30] For the synthesis of PdCu and AuCu NCs, 9 mL OLA, 10 µL OA, 50 µL of TOP and 0.1 mmol of each metal ion precursor (*i.e.*, $Cu(ac)_2$, $PdBr_2$ and $Au(ac)_3$) were mixed in a 100 mL round bottom flask (RBF). In the synthesis of AuPd NCs, only 9 mL OLA and the metal ion precursors (*i.e.*, $Au(ac)_3$ and $Pd(hfacac)_2$) were used, thereby omitting OA and TOP in the synthesis. The mixed metal ion precursor solutions were heated to 110 °C at a heating rate of 6 °C/min under air for 30 min, while stirring at 400 rpms until the metal precursors were dissolved. Afterwards, the solutions were heated to 235 °C at a heating rate of 6 °C/min and were maintained at this temperature for 1 h. The solutions were cooled to room temperature. The resulting solutions were added to centrifuge tubes with 20 mL hexane and were spun at 10,000 rpms for 10 mins to precipitate the NCs. The NCs were washed with a 3:1 ratio of ethanol:hexane three times, and eventually they were suspended in 5 mL of acetone. After washing, the resulting NCs were either supported by drop-casting onto a microscope glass slide (VWR) or supported on disordered carbon with a 50 wt.% metal loading prior to the gas annealing sequence. The supported NCs were placed in an oven, heated to 300 °C at a heating rate of 10 °C/min and left at 300 °C for 30 minutes in a gas sequence of argon (Ar), oxygen (O_2), carbon monoxide (CO) and hydrogen (H2). The choice of temperature during the gas treatments was based on considering the commonly used temperatures in catalytic relevant reactions such as CO_2 hydrogenation (i.e., 250-350 °C), and the stability of the glass support.[31-34] The same procedure was done for a pure disordered carbon sample to obtain a background sample for the following PDF analysis. Hereto note that all the gas-exposed glass- and carbon-supported samples were exposed to air after gas treatment to allow for transfer to relevant characterization equipment.

Powder X-ray diffraction

For the glass-supported NCs, *ex situ* PXRD measurements were performed prior to gas annealing (denoted pristine) and after each gas exposure to track observable changes in their crystal structure. The PXRD patterns were collected on a Bruker D8 instrument using Cu K_α radiation in the angular 2θ-range from 20-80°.

Rietveld refinements of PXRD data were performed using the *Fullprof suite* program package.[35] The peak profiles were described by the Thompson-Cox-Hastings pseudo-Voigt function, where the *Y*-parameter was used to describe the crystallite size-related peak broadening. The background was modelled using linear interpolation between points with refinable heights. All site occupancies and positions were kept fixed at database values during the refinement, and all atomic displacement parameters (ADPs) were fixed at 0.3 Å^2. The unit cell parameter, scale factor, background point heights, and the profile parameter, *Y*, was refined.

Pair distribution function analysis

Data acquisition. X-ray TS measurements were conducted at beamline 11-ID-B, Argonne National Laboratory, APS. The carbon-supported NC samples were packed in Kapton capillaries (from Cole-Palmer) with an outside diameter of 1.05 mm and a wall thickness of 0.025 mm. For each gas used, a pure carbon sample, which had been exposed to the same gas, was packed and used to ensure a correct background for the background subtraction. TS data were collected at ambient conditions in transmission geometry using a Perkin-Elmer detector with a pixel size of 200×200 µm and an X-ray wavelength of 0.211 Å. The sample-to-detector distance and instrumental broadening (Q_{broad}=0.038 Å^{-1} and Q_{damp}=0.010 Å^{-1}) were calibrated using a CeO_2 standard. *Fit2D* was used to calibrate the experimental geometry parameters and azimuthally integrate the scattering intensities to 1D scattering patterns.[36, 37]

PDF modelling. The X-ray TS data were Fourier transformed with *xPDFsuite* to obtain PDFs using a Q_{min} of 0.1 Å^{-1} and a Q_{max} of 25.0 Å^{-1}.[38] The background correction was performed by subtracting the scattering signal obtained from a pure disordered carbon sample, which had undergone the same gas-temperature treatment as the sample in question. Modelling of the experimental PDFs was done using *PDFgui* in the *r*-range from 1-60 Å, in which a least-square optimization procedure was performed between a theoretical PDF and the experimental PDF.[39] The refined parameters included the unit cell parameters, the δ_2-parameter describing local correlated atomic movement, scale factor, a spherical particle diameter, and the isotropic atomic displacement parameters for the atoms in the given structures.

High-resolution transmission electron microscopy

HR-TEM Imaging. For the HR-TEM, Ar- and O_2-exposed PdCu and AuCu NCs supported on disordered carbon were investigated. HR-TEM images were acquired using an image aberration-corrected FEI Titan ETEM equipped with a differentially pumped vacuum column and operated at 300 keV in the broad-beam HR-TEM mode with a spherical aberration coefficient (after correction) of -19.7±3.3 µm for AuCu NCs, and -18.4±5.5 µm for PdCu NCs.[40, 41] Samples for *in situ* observations were prepared by sonicating a suspension of ethanol mixed with the different catalyst powder, including O_2-exposed PdCu and AuCu NCs supported on carbon. The suspensions were drop-casted directly onto separate NanoEX MEMS devices enabling direct heating of the specimens to a temperature estimated by manufacturer supplied calibrations.[42] The samples were introduced into the microscope base vacuum below *ca.* 1×10^{-6} mbar. For the reduction reactions a pressure of 1 mbar H_2 was introduced into the differential pumping system and the samples were heated to 350 °C. Images were acquired using a GATAN K3 camera operated in counting mode with an image pixel size of 0.06 nm (PdCu) and 0.03 nm (AuCu). A stack of 20-30 images were acquired, aligned and summed for each presented TEM image. To minimize beam damage during the *in situ* reduction reactions a dose rate of 20-50 e/(Å^2·s) was used with a total acquisition time om 30 s. The samples were observed to remain stable as function of time under isothermal conditions, suggesting that the electron beam effects were minimal.

Data analysis. The crystallographic phases in the NCs were identified from the crystal lattice fringe spacings observed in the HR-TEM images. Specifically, a fast Fourier transform (FFT) of the entire image displays the reciprocal lattice spacings. If the lattice spacings are unique, compared to the other possible phases, the crystallographic phase can be determined solely from the position of the spots. This was the case for the PdCu samples. Moreover, by masking individual spots in the FFT and creating an inverse FFT (iFFT), the spatial position of the crystal with the specified lattice fringe can be identified in the real space HR-TEM image (see **Fig. S17c-d**). If the lattice spacing was not unique, an FFT of the small region found from the masking procedure was created and the resulting patterns analysed using CrystalMatch and CrystalMaker to find the zone axis (see **Fig. S17e-f**).[43, 44] This was the case for the AuCu samples. Further details can be found below.

Density functional theory calculations

Density functional theory (DFT) calculations were performed to establish the relative stabilities of Au, Cu, and Pd pure metals in the various gas environments. *O, *CO, and *H adsorbates were relaxed to forces below 0.05 eV/Å on fcc (111) terminated surfaces, four-atom layered slabs with coverages of 1/3, 2/3, and 1 monolayer, respectively. Energies were calculated with the revised Perdew-Burke-Ernzerhof (RPBE) exchange-correlation functional and plane-wave expansion of the wave functions using the GPAW code and ASE for atomic manipulations.[45-48] Free energy contributions were simulated assuming ideal gas behaviour for the molecules H_2, CO, and O_2, and assuming harmonic degrees of freedom for the adsorbates. For all details, the structures and scripts necessary for reproducing the DFT calculations have been made freely accessible.[49]

Results and discussion

Initial insights into the gas-induced structural changes of metallic NCs

We start out by considering bulk structural changes induced in monometallic NCs upon gas treatment. PXRD data from Pd, Au and Cu samples, drop-casted onto a glass slide, and subjected to gas treatment are presented in **Fig. 1**. Calculated PXRD patterns of the expected fcc structures are shown below the experimental PXRD patterns. **Fig. 1a** presents the bulk structural response of monometallic Pd NCs, where the pristine state as expected agrees with an fcc Pd structure. The broad reflections and a slight peak movement to lower angles suggest that the Pd NCs are relatively small with a slightly larger unit cell than that of bulk fcc Pd, displayed in **Fig. 1a**. The observation of a unit cell that deviate from the bulk value is often encountered for small NCs due to increased surface exerting on the NCs, which either causes an expansion or contraction of the unit cell depending on the crystal symmetry.[50-53] The larger unit cell is confirmed from Rietveld refinement, which reveals a unit cell parameter of 3.98 Å compared to the expected value of 3.88 Å, and the crystallite size (*i.e.* the crystallite radius) refines to 3.28 nm (see Supplementary Information (SI) **Fig. S1** and **Table S1**).[54] Exposure to Ar at 300 °C does not induce any bulk structural modifications as observed by the constant position of the resulting Bragg peaks in **Fig. 1a** and from the Rietveld refinement (see SI **Fig. S1** and **Table S1**). However, as the gas environment is changed to O_2, significant structural changes are observed. The presence of O_2 induces an oxidation of the Pd NCs with the formation of a tetragonal PdO phase, leaving only a small amount of unreacted metallic Pd.[55] Using these structure models in a two-phase Rietveld refinement reveals a respective PdO-to-Pd phase composition of 86.5% to 13.5%, and with unit cell parameters comparable to that of the bulk structure values (see SI **Fig. S1** and **Table S1**).[55] Even though two phases are used to describe the NCs, the oxidation is expected to occur on the NC surface, leaving a core-shell particle rather than separate Pd and PdO NCs. As the NCs are exposed to CO, the NC structure is found to reverse back into the pure fcc Pd structure observed in the pristine state. This has previously been observed for reduction of PdO(101) using CO, where metallic Pd(111) domains were found to form with the co-formation of CO_2.[56] However, by comparing the diffraction patterns resulting from the pristine and CO-exposed Pd NCs, a clear change in the peak profile and position is observable. The sharper peak profile displayed from the CO-exposed Pd NCs indicates growth of the Pd NCs (the refined crystallite size was 14.96 nm as compared to 8.09 nm for the O_2-exposed NCs), while the change in peak position reveals a smaller unit cell (see SI **Fig. S1** and **Table S1**). By further exposure to H_2, a slightly sharper peak profile and constant peak position is observed, which suggests continuous growth from sintering of the Pd NCs (the refined crystallite size was here 24.51 nm) without inducing changes in the unit cell parameters. The discussed transformations are schematically presented in **Fig. 1g.**

As seen in **Fig. 1b**, the pristine Cu NCs exhibit fcc Cu structure with unit cell values comparable to bulk fcc Cu (see SI **Fig. S1** and **Table S2**).[57] However, sharp peaks are observed at low 2θ-values (2θ<30°), which cannot be identified as originating from fcc Cu or from possibly relevant structures such as carbonates and silicates, when compared to calculated PXRD patterns from the database (see **Fig. S2**). Instead, these peaks are most likely related to unreacted Cu^{2+} precursor. Exposure to Ar induces growth of the Cu NCs from 27.57 nm to 55.15 nm according to the Rietveld refinement. Again, O_2-exposure causes oxidation of the metallic Cu, where two oxide structures are formed: CuO ($C2/c$) and Cu_2O ($Pn\overline{3}m$). The very broad character of these peaks indicates that either very small NCs are formed or that the structure is partly amorphous. Rietveld refinement presents a CuO/Cu_2O phase composition of 33.70%/66.30% with unit cell parameters comparable to that of the bulk values.[58, 59] The crystallite sizes refine to 6.09 nm and 2.42 nm for CuO and Cu_2O, respectively. Exposure to CO eliminates the presence of CuO due to reduction, while the Cu and Cu_2O peak intensities increase. This is also clearly observed from the Rietveld refinement, where the reduction of CuO results in 25.45% metallic fcc Cu (see SI **Fig. S1** and **Table S2**). Simultaneously, the peak width of the Cu_2O-identified Bragg peaks decreases, indicating growth of the Cu_2O NCs, which is also evidenced from the Rietveld refinement (refined crystallite size 12.79 nm). Upon exposure to H_2, the NC structure reverses back into the pristine fcc Cu structure with no remaining Cu_2O observed. **Fig. 1g** shows a schematic representation of the observed transformations.

Finally, Au NCs were treated with the same varying gas environments. As clearly illustrated in **Fig. 1c** and in the Rietveld refinements (see SI **Fig. S1** and **Table S3**), no structural changes can be observed in any of the different gas environments, where both peak positions and peak widths are maintained throughout the gas and heat exposures. It is well-known that bulk gold is chemically inert with reported catalytic activities much lower than those of Pd metal.[60, 61] It has previously been reported that the catalytic activity of Au NCs can be greatly increased by reducing the NC diameter.[62, 63] This relation has been attributed to the increase in the number of undercoordinated surface atoms.[64, 65] However, as seen from the sharp peak profile in **Fig. 1c** and the Rietveld refinements (see SI **Fig. S1** and **Table S3**, the Au NCs synthesized here are significantly larger than the previous reported Au activity studies of only a few nanometres (refined sizes between 14-25 nm). As a result, we cannot rule out that the inertness of the NCs might be related to the larger NC size, whereby the properties most likely follow the trends known from bulk Au.

Having established how the monometallic NCs behave separately under varying gas environments, we turn to the bimetallic NCs with the resulting PXRD patterns presented in **Fig. 1d-f**. As instantly seen in **Fig. 1d-f**, the incorporation of a second metal greatly changes the structural response to the gas environment. As seen in **Fig. 1d-e**, **Fig. S3** and **Tables S4-S5**, the pristine and Ar-exposed structures of PdCu and AuCu take the intermetallic structures denoted B2 and $L1_0$, respectively.[66, 67] Upon O_2-exposure, the B2 PdCu and $L1_0$ AuCu NCs undergo the first observable structural change. As PdCu NCs are exposed to O_2, a PdO phase is formed as also seen for the monometallic Pd

NCs. Although the schematic illustration in **Fig. 1h** presents PdO as a separate NC, the PdO phase is most likely to be present on the surface of the NCs. For the AuCu system, an fcc Au phase is found to form upon oxidation. Interestingly, for both PdCu and AuCu, we see no Bragg peaks from any crystalline copper oxide or metallic Cu phase. This observation suggests that an amorphous Cu-containing phase may form after oxidation. When further treating the samples in CO and H_2 atmospheres, the Cu appears to reincorporate itself into a crystalline phase, forming bimetallic PdCu and AuCu structures with an increased NC size as evidenced from the refined crystallite sizes in **Table S5**. In the case of PdCu, the initial intermetallic B2 structure is only partly recovered (*i.e.* 47.38%), as a disordered A1 alloy phase ($PdCu_{fcc}$ seen in **Fig. 1d**) appears (*i.e.* 52.62%).[68] In the AuCu system, a small amount of an fcc Au phase remains along with the intermetallic $L1_0$ AuCu phase and a Au_3Cu phase upon CO- and H_2-exposure (see **Fig. 1e**, **Fig. S3** and **Table S5**). Contrary, the AuPd system is found not to undergo any significant structural changes in the varying reactive atmospheres as displayed in **Fig. 1f**. Instead, the AuPd system can be described by an fcc AuPd and fcc Au phase, where the relative ratio between the two phases slightly changes throughout the gas- and heating treatments (see SI **Fig. S3** and **Table S6**). Furthermore, a sharp diffraction peak at 30° 2θ can be observed in both the AuPd and AuCu system as highlighted in **Fig. S4**, which suggests that the peak either relates to Au or the SiO_2 substrate. Comparing with relevant structures from the database such as SiO_2, carbonates, Au_2O_3 and $Au_{10}Si_3$ could not describe this structural feature. We therefore suspect that the peak relates to unreduced Au^{3+} precursor in the synthesis, although we have not been able to identify which structure it arises from.

Based upon the *ex situ* PXRD study, we see significant differences in the structural responses between the mono- and bimetallic structures when exposed to varying gas environments and heat. Most importantly, the Cu species present in the bimetallic structures "disappear" from the crystalline phases in O_2, but are recovered upon introducing reducing gas conditions. However, as a consequence of the quality of the in-house PXRD measurements, detection of the possibly small, nano-crystalline or amorphous Cu-containing NPs upon oxidation is limited. Thus, to allow identifying the role of Cu in the oxidized Cu-containing bimetallic structures, synchrotron-based *ex situ* X-ray TS with subsequent PDF analysis was introduced.

PDF analysis of the gas-induced changes of metallic NCs

The gas annealing cycle was slightly altered for the samples prepared for X-ray TS measurements resulting in the following order: Pristine-Ar-CO-O_2-H_2. This change allowed us to observe the transformation from the fully oxidized O_2-treated NCs to the fully reduced NCs formed under the most commonly used reducing atmosphere, thereby circumventing the intermediate reduction step using CO. Furthermore, the NC support material was changed from glass slide to disordered carbon. Disordered carbon was chosen due to the low scattering power of carbon and its amorphous structure, thereby lowering the contribution of the support to the scattering signal. We note that disordered carbon is known to undergo rapid graphitization upon high temperature treatment and that the presence of metallic species has been shown to accelerate this process.[69] Although the temperature in our study is well below the reported temperatures used in these treatments (*i.e*. 1400 °C), we examined whether graphitization should be considered in the samples. By using Raman spectroscopy, we found that the exposure to either a reducing atmosphere at elevated temperatures or the presence of metallic Pd did not alter the disordered carbon sample in any significant way, which meant that graphitization or increase in disorder was ruled out (see **Fig. S5** and Section C in SI for details).

Fig. 2 shows the X-ray TS data of the monometallic Pd and Cu NCs annealed in the various gas environments. The reduced structure functions $F(Q)$ are plotted in **Fig. 2a**,**e.** As expected from the PXRD analysis, sharp scattering peaks in reciprocal space, *F(Q),* are observed for all three monometallic samples, showing the presence of crystalline particles.

For the supported Pd NCs in **Fig. 2a**, a Pd fcc structure can be identified for the pristine, Ar- and CO-exposed Pd NC samples, when compared to the calculated $F(Q)$ patterns. As also observed in the PXRD experiments, an oxidizing atmosphere promotes the formation of PdO, while a significant amount of the fcc Pd phase remains. Exposure to H_2 converts the PdO into metallic fcc Pd. The observed changes can also be followed in real space by investigating the reduced PDF, *G(r)*, as displayed in **Fig. 2b**. For the pristine, Ar- and CO-exposed Pd NC samples, the Pd fcc structure can again be identified in real space with a nearest neighbour Pd-Pd bond distance at 2.80 Å. Additionally, the formation of PdO is observed by the presence of Pd-O and Pd-Pd bond distances at 2.02 Å and 3.03 Å, respectively, as illustrated in **Fig. 2b**. From PDF refinements in **Fig. 2c**, it is observed that the pristine Ar- and CO-exposed Pd NC samples share a similar unit cell parameter of 3.99 Å (see also **Fig. S6** and **Table S7**). This is again significantly larger than the bulk Pd fcc unit cell parameter, however, small NCs are known to often exhibit expanded unit cell dimensions.[51, 52]

The PDF can also be used to estimate crystallite sizes of the coherently scattering domains by examining the extent of oscillations in real space. From the PDF refinements (see SI **Fig. S6** and **Table S7**), it is observed that only the final exposure to H_2 results in a significant increase of the NC size, as opposed to the observations when using PXRD. We note, however, that the rapid acquisition PDF (RA-PDF) geometry used for the TS measurements results in significant instrumental Bragg peak broadening, which increases the uncertainties on the refined crystallite diameter in the size range above 5-10 nm. This is also evident when comparing the crystallite sizes determined from PDF and PXRD (see **Tables S7** and **S1**, respectively), where slightly larger NC sizes are reported based on the PDF refinements. However, general trends of NC growth can still be extracted from the resulting PDF refinements. In addition, it is also important to note that the sizes obtained from the fits are possibly underestimates of the actual particle size. The underestimation originates from the fact that PDF (and PXRD)

probes the volume weighted coherent scattering domains within the NCs, while TEM images particles directly. As the particles might be polycrystalline and thereby consist of many domains, the resulting size probed with TEM will be larger.

The X-ray TS data in **Fig. 2** also confirm the formation of an oxide phase in an oxidizing environment for the monometallic Cu samples. In **Fig. 2e**, the reciprocal space data show a pristine sample containing both an fcc Cu phase and a CuO phase. This is also evidenced from the PDF refinements in **Fig. 2h** (see also **Fig. S6** and **Table S8** in SI). Here, we found that the best description of the data was obtained if two different CuO phases, with different crystallite diameter sizes of 1.51 nm and 3.67 nm, respectively, were introduced. This refinement strategy accounts for a large size distribution and a possible surface-located CuO phase on the metallic Cu NCs. As the sample is exposed to Ar, the Bragg peaks related to CuO decrease, while a Cu_2O phase form. In the PDF data of **Fig. 2f**, this is observed from the contraction of the Cu-O bond (1.96 Å in CuO and 1.85 Å in Cu_2O)[58, 70], as well as from the appearance of an expanded Cu-Cu distance at 2.99 Å, which is present in Cu_2O. As the atmosphere is changed to O_2, the amount of the Cu_2O phase decreases with the additional formation of CuO, while metallic Cu is still present in the sample.

As presented in **Fig. 2f**,**h**, **Fig. S6** and **Table S8**, the O_2-exposed Cu NC sample is described by the two CuO phases as in the pristine state, a small amount of metallic Cu and a Cu_2O phase. However, although the PDF peaks at high *r*-values are well-described (*i.e*. *r*>15 Å), there is still a significant mismatch in the local range (*r*<10 Å). This suggests that even more disorder is present in the NCs than accounted for. Indications of this might also be found in the refinements of the O positions in the nano-structured CuO structure, which highly deviate from the reported bulk O positions (see **Table S8** in SI).[58] Although the refinement includes three separate phases, i.e. CuO, Cu_2O and Cu, the Cu oxide phases are likely to be located on the surface of the Cu NCs than as separate oxide NCs. Finally, H_2-exposure results in an fcc Cu phase with only a minor Cu_2O component as evident in both reciprocal- and real space, which is accompanied by a slight increase in NC size as observed in **Fig. 2f**, **Fig. S6** and **Table S8**.

When exposing Au NCs to the various gas environments, the NCs are again found to be unaffected as observed in **Fig. S7a-d**. This is clearly observed from the PDF refinement, where only an increase in NC size is found to result from the gas exposure (see **Fig. S6** and **Table S9** in SI). The observed NC growth is illustrated in **Fig. S7e**.

We have now evaluated how the individual monometallic supported components respond in the various gasses and how these responses can be observed with X-ray TS. Next, we investigate the structural response of PdCu, AuCu and AuPd to identify the role and dynamic behaviour of Cu in binary NCs.

Fig. 3 displays the structural changes of the bimetallic PdCu NCs in both reciprocal and real space. As expected, the pristine supported PdCu NCs take the intermetallic B2 PdCu structure as seen in **Fig. 3a**. However, a small asymmetry of the peak at 2.98 $Å^{-1}$ in reciprocal space is observed, which relates to the presence of a small amount of monometallic fcc Pd. The larger fraction of Pd compared to Cu is also corroborated by ICP-OES measurements (see SI **Table S13**). The monometallic Pd formation is further confirmed when modelling the PDF in **Fig. 3c**. Interestingly, as the B2 PdCu NCs undergoes O_2-exposure, significant changes can be observed. If considering first the reciprocal space data, Bragg peaks from a metallic Pd phase first appears. The formation of a pure Pd phase upon O_2-exposure is also clearly identified in the PDF as illustrated in **Fig. 3b**. Here, the emergence of peaks at 2.75 Å, 3.88 Å and 5.49 Å relates to Pd-Pd bond distances in metallic Pd. However, we also observe a broad peak in the *Q*-space data, which agrees with the formation of small CuO nanoparticles. Indications of this phase is also observed in the PDF from the appearance of Cu-O and Cu-Cu interatomic distances. The formation of a CuO phase is not only in accordance with the observed monometallic Cu behaviour as seen in **Fig. 2e**, but also with the known oxophilicity of Cu. Here, the associated increase in Cu-O bond strength is reported to promote an CuO phase.[71] As also observed in **Fig. 3a**, only a small signal from the B2 PdCu phase remains after exposure to the oxidising atmosphere. Refining the PDF in **Fig. 3d** shows that only 10% of the B2 PdCu is left in the NC sample together with the major phase of metallic Pd with different crystallite diameter sizes to account for the polydispersity (Pd_{bulk} correspond to 39% and Pd_{nano} 20%) and the remainder corresponds to CuO (31%) after O_2-exposure. The TS data and PDF thus allows us to identify some of the Cu, which can be described as a nanocrystalline CuO-phase with a crystallite diameter of *ca.* 4 nm.

The PDF also reveals that the NC sizes of the identified phases are heavily impacted by the O_2-exposure. While a relatively constant NC diameter of both the B2 PdCu and Pd phases from the pristine to CO-exposed NCs are observed (*i.e.* 7.0 nm and 1.5 nm, respectively), the O_2-exposure results in a decrease of the B2 PdCu NC size, while the Pd NCs both increase in size and exhibit a polydisperse size distribution (see **Fig. S8** and **Table S10**). Upon the subsequent H_2-exposure, the B2 PdCu structure is recovered, and the particles have significantly grown in diameter (25 nm *vs.* 7 nm for the pristine state). At this point, there is only 30% metallic Pd left in the sample. **Fig. 3e** summarizes the discussed phase transformations.

We now consider the AuCu samples. Both the pristine structure and the samples exposed to Ar and CO can be described as a phase mixture of $L1_0$ AuCu and a metallic fcc Au phase, as illustrated in **Fig. 4a-b**, which is further corroborated by ICP-OES measurements (see SI **Table S13)**. As the NCs undergo O_2-exposure, the $L1_0$ AuCu phase converts into an Au_3Cu phase upon Cu exclusion, while the fcc Au phase remains. A small peak at 2.50 $Å^{-1}$ suggest the formation of nanocrystalline CuO. The PDF refinements reveals that the AuCu NCs after O_2-exposure can be described as 59% Au_3Cu, 36% fcc Au and 5% CuO with crystallite sizes of 5.1 nm, 6.9 nm and 2.3 nm, respectively (see **Fig. S8** and **Table S11** in SI). However, it is clearly still difficult to precisely track what happens with Cu in the NC sample, as only a small percentage of the initial Cu can be identified as CuO. The difference between the X-ray scattering power of Au and Cu means that the Au phases dominate the PDF, and thus

complicates further analysis of identifying the structure of a possible disordered Cu oxide phase with a small particle size. When the NCs are exposed to reducing conditions in H_2, the Au_3Cu reconverts to the $L1_0$ AuCu phase with a crystallite size comparable to the pristine NCs (6.5 nm for H_2-treated vs 5.5 nm for the pristine state), while small fcc Au NCs remain (4.2 nm for H_2-treated *vs.* 6.9 nm for O_2-treated, see **Fig. 4a-b, Fig. S8** and **Table S11**). This observation suggests a high degree of mobility associated with Cu in the structures, which enables reconversion of the non-crystalline segregated Cu-structure into the initial intermetallic structure.

Finally, we turn to the supported AuPd NCs in **Fig. S9**. As also observed from the PXRD experiments, no structural changes are induced during exposure to the various gas environments, which is contrary to previous experiments reporting a Pd surface enrichment under CO exposure.[14] The lack of structural response could indicate that the restructuring of Pd in the various gas environments is retarded in the presence of Au. A hypothesis supporting this immobilisation of the Pd response could be related to a possible surface termination of Au on the surface, inhibiting the gas molecules to interact with underlying Pd.[72] From the PDF refinements it is found that the AuPd NC samples contain approximately 20% metallic Au (see **Fig. S9c-d**, **Fig. S8** and **Table S12**), which is also illustrated in **Fig. S9e**. Therefore, it might be that some of this monometallic Au provides the suggested surface coverage to prevent Pd surface segregation and oxidation.

Imaging the dynamics of bimetallic NCs

From the PXRD and TS experiments, it is clearly observed that exposing the mono- and bimetallic structures to oxidizing and reducing environments results in significant structural changes. However, the exact role and dynamics of Cu is still challenging to fully elucidate and would benefit from real space visualization. HR-TEM was therefore used to observe the structural distribution and evolution of the carbon-supported Cu-composed bimetallic NCs during exposure to a reactive gas environment. Specifically, HR-TEM images were acquired on selected O_2-treated NCs during exposure to a reducing environment established by adding 1 mbar H_2 to the sample region and heating up to 350 °C. The crystallographic phases in the TEM images were identified from the lattice fringe spacings and their spatial distribution across the projected area of the crystal in the HR-TEM image were revealed through Fourier analysis. **Fig. S10-S12** shows corresponding Fast Fourier transforms (FFTs) for the Ar-exposed PdCu, O_2-exposed PdCu and H_2-exposed PdCu NCs. The crystalline phases identified from these regions on the NCs were colour coded and superimposed as transparent maps to indicate the spatial phase distribution on the NCs. To provide a complete picture of the NC phase distribution, we initially determined the structures of both the Ar- and O_2-treated supported NCs prior to reduction using HR-TEM.

For the supported PdCu NCs, the intermetallic B2 PdCu structure could be assigned to the Ar-treated sample structure solely based on the lattice spacing as displayed in **Fig. 5a** (see also **Fig. S10** and **Table S14** for the relevant lattice spacings). The distribution of the B2 PdCu phase ($Pm\bar{3}m$) across the PdCu agglomerate is indicated by the green colour in **Fig. 5a**, which shows the B2 PdCu phase being present throughout the agglomerate. Identification of the B2 PdCu structure agrees with the previous observation provided by PXRD and PDF (see **Fig. S8** and **Table S10**). **Fig. 5a** also shows contrast variations on the scale of 10-20 nm suggesting the depicted structure is an agglomerate of smaller NCs, which is consistent with the average crystal sizes of 7-8 nm determined by PXRD and PDF (see **Table S4** and **S10**, respectively).

From the X-ray TS data in **Fig. 3** it was noted that exposure to an O_2 atmosphere resulted in the presence of a disordered CuO phase with a small domain size. Keeping this apparent CuO segregation in mind, we turned to the O_2-treated PdCu sample to examine the location of CuO. As seen in **Fig. 5b**, the HR-TEM image allows identifying a CuO (*C2/c*) phase on the surface on the NCs as visualized by the red colour (see also **Fig. S11)**. By looking at the surface regions in **Fig. 5b**, where CuO is identifiable and highlighted in red, the image exhibits a contrast compared to the interior of the NCs corresponding to a decrease in mass-thickness upon oxidation. This indicates that CuO is present at the surface. Further analysis of the interior of the agglomerate was limited due to the lack of resolved lattice fringes resulting from NC sintering, thereby leaving regions too thick to resolve. Afterwards, the O_2-treated PdCu NCs were exposed to the reducing H_2 environment in the electron microscope. First, the HR-TEM indicates an absence of CuO, since the reduced contrast in the edge-regions and the CuO lattice fringes have vanished (see **Fig. 5c** and **S12**). Interestingly, the bulk contrast extends to the edge of the agglomerate. Lattice fringes corresponding to the B2 PdCu crystal structure appear both at the edge as well as in the bulk regions as highlighted by the green colour. This indicates that the CuO is reduced, and the B2 PdCu crystal phase recovered.

These *in situ* HR-TEM observations of the PdCu NCs suggest that upon O_2-exposure, Cu segregates towards the surface forming an CuO phase, while the interior is enriched with Pd. The formation of a stable surface segregated CuO phase is also in line with Gibbs free energy calculations as shown in **Fig. S16**. The following exposure to H_2 reduces the Cu^{2+} from the oxide phase, which may recombine with Pd found in the interior to restore the favourable Pd-Cu bonds in the B2 PdCu structure. Thus, Cu can dynamically respond to the gas environment by in a reversible manner migrate between the bimetallic NC bulk and surface.

When turning to the supported intermetallic $L1_0$ AuCu NCs, a slightly different behaviour is observed. Due to the similar lattice spacings of the previously identified structures from PXRD and PDF (see **Table S14** for the relevant lattice spacings listed), identifying the phases solely based on the FFTs could not be done (see **Fig. S13-S15**). Instead, the procedure of identifying the NC structures was slightly altered by following the process schematically presented in **Fig. S17**.

First, the spatial positions of the individual crystals were localized. This was done by masking each spot in the FFT and creating a corresponding inverse FFT (iFFT) (see **Fig. S17b-c**). By creating a new FFT from only this region, a pattern from the single crystal is formed (**Fig. S17d-e**). This pattern was then analysed using CrystalMaker to find the phase and zone-axis, the two of which enables the local crystal structure to be identified (**Fig. S17f**). This procedure was done for all crystals in the image (see **Fig. S18** for details).

Fig. 5d presents the Ar-treated carbon-supported AuCu NCs. Due to the similar lattice spacings of CuO (*C2/c*) and $L1_0$ AuCu, ($Pm\bar{3}m$) separate identification of these two phases could not be done, thereby leaving the Ar-treated AuCu NCs as described by $L1_0$ AuCu phase and/or CuO phase (highlighted in purple in **Fig. 5d**). As **Fig. 5e** illustrates, several phases can be identified in the O_2-treated AuCu NCs. These phases include monometallic fcc Au ($Fm\bar{3}m$) (green) and CuO (red). However, within some regions, distinction between an Au and CuO phase could not be resolved as highlighted by the yellow areas. Despite this lack of distinction, significant high-resolution information can be observed in the NCs in **Fig. 5e**, which is further highlighted in **Fig. S19.** Contrary to the behaviour observed in the supported PdCu NCs, the CuO does not show a preferential location on the surface of the O_2-treated NCs, but are rather present as projected areas suggesting that distinct CuO NCs form. It is, however, interesting to note, that there is a rather random distribution of small neighbouring domains composed of either CuO or Au in the NCs. Upon reduction in H_2, as shown in **Fig. 5f**, the NCs again sharpen around the edges and loose ill-defined character surrounding the edges. After H_2-treatment, an $L1_0$ AuCu structure is now able to describe the NC structure as spatially indicated by the blue colour in **Fig. 5f**. Furthermore, it is especially important to note that neighbouring Au and CuO domains in the NC are fully converted into the $L1_0$ AuCu structure, thereby essentially depleting CuO regions. This appear to occur while the AuCu structure remains identifiable within sharply contrasted and well-defined NC boundaries. This indeed strengthens the hypothesis of Cu-facilitated mobilization in the NCs upon exposure to varying gas environments.

Conclusions

In summary, we have provided detailed structural information concerning the effect of the reactive gas environment on the atomic-scale structure of catalytically active mono- and bimetallic NCs. We have hereby demonstrated the importance of characterizing and retrieving the structural information from a dynamic, non-pristine state to completely understand the origin of the observed catalytic properties.

Through PXRD and X-ray TS experiments on Au, Cu, Pd, PdCu, AuPd and AuCu NCs, we observed significant bulk changes of the NCs when placed in a sequence of Ar, O_2, CO and H_2 environments at 300 °C. By employing PXRD, we observe that exposure of monometallic Pd and Cu NCs to O_2 resulted in formation of oxides of both metals, followed by recovery of metallic Pd and Cu upon exposure to a reducing atmosphere. However, when a second metal was incorporated forming PdCu and AuCu NCs, the response to the environment changed. Both PdCu and AuCu showed a loss of metallic Cu in the crystalline phases present after exposure to O_2, where only Bragg peaks from Pd and Au remained observable. This indicate that an amorphous or nanostructured Cu-containing phase forms. When further treating the NCs in reducing atmospheres, the Cu "reappeared" and reincorporated itself, thereby forming the initial bimetallic structures. Contrary, the AuPd alloy system displayed static structural behaviour when varying the reactive atmospheres; no distinct bulk structural changes were observed. Thus, these observations clearly illustrated that the bimetallic response to the gas environments cannot simply be considered as a combination of the behaviours seen in the individual monometallic systems. Instead, new properties arise when we combine metals in a bimetallic structure. Further analysis using X-ray TS and PDF analysis showed that PdCu and AuCu NCs in an oxidizing environment both formed CuO phases along with either monometallic Pd or Au, respectively. However, in these instances the CuO scattering signal was less dominant and displayed broad features in the TS patterns. This could either suggest small, disordered CuO NCs or the presence of CuO surface segregation.

Use of *in situ* HR-TEM enabled us to image the location of CuO. For the supported PdCu NCs, the CuO phase formed upon O_2-exposure and could be located on the surface of the NCs. However, for the AuCu system, small segregated and randomly distributed bulk CuO and Au domains comprised NC agglomerates. Upon H_2-exposure, CuO depleted and Cu-containing intermetallic structures were recovered for both PdCu and AuCu NCs. Combining these observations with PXRD and X-ray TS suggest that in binary Cu-containing NCs, Cu is the more mobile component under oxidation and reduction conditions, and that Cu mobilization dominates segregation with formation and dissolution of CuO.

These results leave us with new insights into the dynamic behaviour of NC catalysts, which will be highly relevant when we turn to actual catalytic reaction conditions. Understanding the origin of structural changes induced in the metal NCs under single gas environments may furthermore aid in deducing any gas-induced structural changes taking place in mixed gas reaction conditions. As clearly observed, new properties arise when we combine metals in a bimetallic structure differing significantly from their monometallic counterparts. The question is if we through careful investigation can describe these properties in a unifying framework to tailor nanocatalysts with specific desirable properties.

Author Contributions

J.K.M., K.D.J., J.R. and K.M.Ø.J. conceived the project. J.K.M. synthesized the samples, while J.K.M. and K.D.J. annealed the samples. J.K.M. performed the PXRD experiments, and refined the PXRD and TS-PDF data. S.C.F. performed the *in situ* HR-TEM experiments and data analysis with inputs from S.H. J.K.P. performed the Gibbs free energy calculations, and T.V. performed Raman experiments. J.K.M. and S.C.F. wrote the

manuscript with inputs from all authors. K.M.Ø.J. and J.R. supervised the project.

Conflicts of interest

There are no conflicts to declare.

Acknowledgements

The authors would like to acknowledge the staff of beamline 11-ID-B for experimental assistance. This research used the mail-in program at Beamline 11-ID-B of the Advanced Photon Source, a U.S. Department of Energy (DOE) Office of Science User Facility, operated for the DOE Office of Science by Argonne National Laboratory under Contract No. DE-AC02-06CH11357. J. K. M and K. M. Ø. J. are grateful for funding from the VILLUM FONDEN through a Villum International Postdoc Grant (VIL41388) and Villum Young Investigator Grant (VKR00015416), respectively. We acknowledge support from the Danish Ministry of Higher Education and Science (Structure of Materials in Real Time (SMART) grant) and the Danish National Research Foundation Center for High Entropy Alloy Catalysis (DNRF 149). The Center for Visualizing Catalytic Processes is sponsored by the Danish National Research Foundation (DNRF146). K.D.J. would like to thank the Independent Research Fund Denmark for the award of a DFF-Research Project 1 grant (9041-00224B). We would like to thank Tatiana Y. M. Bligaard for performing the ICP-OES measurements.

References

1. I. Mustieles Marin, J. M. Asensio and B. Chaudret, *ACS Nano*, 2021.
2. F. Gao, Y. Wang and D. W. Goodman, *J. Phys. Chem. C*, 2010, **114**, 4036-4043.
3. S. Meenakshisundaram, E. Nowicka, P. J. Miedziak, G. L. Brett, R. L. Jenkins, N. Dimitratos, S. H. Taylor, D. W. Knight, D. Bethell and G. J. Hutchings, *Faraday Discussions*, 2010, **145**, 341-356.
4. P. Liu and J. K. Nørskov, *Phys. Chem. Chem. Phys.*, 2001, **3**, 3814-3818.
5. H. Li, K. Shin and G. Henkelman, *J. Chem. Phys.*, 2018, **149**, 174705.
6. J. Sachtler and G. Somorjai, *Journal of Catalysis*, 1983, **81**, 77-94.
7. S. Zhang, X. Zhang, G. Jiang, H. Zhu, S. Guo, D. Su, G. Lu and S. Sun, *J. Am. Chem. Soc.*, 2014, **136**, 7734-7739.
8. J. Suntivich, H. A. Gasteiger, N. Yabuuchi, H. Nakanishi, J. B. Goodenough and Y. Shao-Horn, *Nature chemistry*, 2011, **3**, 546-550.
9. T. Bligaard and J. K. Nørskov, *Electrochim. Acta*, 2007, **52**, 5512-5516.
10. V. R. Stamenkovic, B. Fowler, B. S. Mun, G. Wang, P. N. Ross, C. A. Lucas and N. M. Marković, *science*, 2007, **315**, 493-497.
11. C. H. Wu, C. Liu, D. Su, H. L. Xin, H.-T. Fang, B. Eren, S. Zhang, C. B. Murray and M. B. Salmeron, *Nature Catalysis*, 2019, **2**, 78-85.
12. E. K. Gibson, A. M. Beale, C. R. A. Catlow, A. Chutia, D. Gianolio, A. Gould, A. Kroner, K. M. Mohammed, M. Perdjon and S. M. Rogers, *Chem. Mater.*, 2015, **27**, 3714-3720.
13. M. A. van Spronsen, K. Daunmu, C. R. O'Connor, T. Egle, H. Kersell, J. Oliver-Meseguer, M. B. Salmeron, R. J. Madix, P. Sautet and C. M. Friend, *J. Phys. Chem. C*, 2018, **123**, 8312-8323.
14. M. Mamatkulov, I. V. Yudanov, A. V. Bukhtiyarov, I. P. Prosvirin, V. I. Bukhtiyarov and K. M. Neyman, *J. Phys. Chem. C*, 2018, **123**, 8037-8046.
15. A. Boubnov, J. Timoshenko, C. J. Wrasman, A. S. Hoffman, M. Cargnello, A. I. Frenkel and S. R. Bare, *Radiation Physics and Chemistry*, 2020, **175**, 108304.
16. A. J. McCue and J. A. Anderson, *Journal of Catalysis*, 2015, **329**, 538-546.
17. F. Gao, Y. Wang and D. W. Goodman, *J. Phys. Chem. C*, 2009, **113**, 14993-15000.
18. H. An, H. Ha, M. Yoo and H. Y. Kim, *Nanoscale*, 2017, **9**, 12077-12086.
19. V. Soto-Verdugo and H. Metiu, *Surface science*, 2007, **601**, 5332-5339.
20. F. Tao, M. E. Grass, Y. Zhang, D. R. Butcher, J. R. Renzas, Z. Liu, J. Y. Chung, B. S. Mun, M. Salmeron and G. A. Somorjai, *Science*, 2008, **322**, 932-934.
21. X. Zhou, W. Xu, G. Liu, D. Panda and P. Chen, *J. Am. Chem. Soc.*, 2010, **132**, 138-146.
22. M. Ouyang, K. G. Papanikolaou, A. Boubnov, A. S. Hoffman, G. Giannakakis, S. R. Bare, M. Stamatakis, M. Flytzani-Stephanopoulos and E. C. H. Sykes, *Nature Communications*, 2021, **12**, 1-11.
23. T. W. Hansen and J. B. Wagner, *Acs Catalysis*, 2014, **4**, 1673-1685.
24. P. L. Hansen, J. B. Wagner, S. Helveg, J. R. Rostrup-Nielsen, B. S. Clausen and H. Topsøe, *Science*, 2002, **295**, 2053-2055.
25. C. Holse, C. F. Elkjær, A. Nierhoff, J. Sehested, I. Chorkendorff, S. Helveg and J. H. Nielsen, *J. Phys. Chem. C*, 2015, **119**, 2804-2812.
26. M. A. Newton, K. W. Chapman, D. Thompsett and P. J. Chupas, *J. Am. Chem. Soc.*, 2012, **134**, 5036-5039.
27. V. Petkov, L. Yang, J. Yin, R. Loukrakpam, S. Shan, B. Wanjala, J. Luo, K. Chapman and C. Zhong, *Phys. Rev. Lett.*, 2012, **109**, 125504.
28. V. Petkov, S. Shan, P. Chupas, J. Yin, L. Yang, J. Luo and C.-J. Zhong, *Nanoscale*, 2013, **5**, 7379-7387.
29. J. T. Gamler, A. Leonardi, H. M. Ashberry, N. N. Daanen, Y. Losovyj, R. R. Unocic, M. Engel and S. E. Skrabalak, *ACS nano*, 2019, **13**, 4008-4017.
30. C. Wang, X. Sang, J. T. Gamler, D. P. Chen, R. R. Unocic and S. E. Skrabalak, *Nano Lett.*, 2017, **17**, 5526-5532.
31. M. S. Frei, C. Mondelli, R. García-Muelas, K. S. Kley, B. Puértolas, N. López, O. V. Safonova, J. A. Stewart, D. Curulla Ferré and J. Pérez-Ramírez, *Nature communications*, 2019, **10**, 3377.
32. D. Heyl, U. Rodemerck and U. Bentrup, *Acs Catalysis*, 2016, **6**, 6275-6284.
33. T.-y. Chen, C. Cao, T.-b. Chen, X. Ding, H. Huang, L. Shen, X.

Cao, M. Zhu, J. Xu and J. Gao, *Acs Catalysis*, 2019, **9**, 8785-8797.
34. J. L. Snider, V. Streibel, M. A. Hubert, T. S. Choksi, E. Valle, D. C. Upham, J. Schumann, M. S. Duyar, A. Gallo and F. Abild-Pedersen, *Acs Catalysis*, 2019, **9**, 3399-3412.
35. J. Rodríguez-Carvajal, *Physica B: Condensed Matter*, 1993, **192**, 55-69.
36. A. P. Hammersley, S. O. Svensson, M. Hanfland, A. N. Fitch and D. Hausermann, *High Pressure Research*, 1996, **14**, 235-248.
37. A. P. Hammersley, *Journal of Applied Crystallography*, 2016, **49**, 646-652.
38. X. Yang, P. Juhas, C. L. Farrow and S. J. Billinge, *arXiv preprint arXiv:1402.3163*, 2014.
39. C. L. Farrow, P. Juhas, J. W. Liu, D. Bryndin, E. S. Bozin, J. Bloch, T. Proffen and S. J. Billinge, *J Phys Condens Matter*, 2007, **19**, 335219.
40. S. Helveg, C. Kisielowski, J. Jinschek, P. Specht, G. Yuan and H. Frei, *Micron*, 2015, **68**, 176-185.
41. J. Jinschek and S. Helveg, *Micron*, 2012, **43**, 1156-1168.
42. L. Mele, S. Konings, P. Dona, F. Evertz, C. Mitterbauer, P. Faber, R. Schampers and J. R. Jinschek, *Microscopy Research and Technique*, 2016, **79**, 239-250.
43. D. C. Palmer, *Zeitschrift für Kristallographie-Crystalline Materials*, 2015, **230**, 559-572.
44. S. B. Simonsen, T. T. Muhl, K. T. S. Thydén, C. Chatzichristodoulou, J. Nielsen and B. R. Sudireddy, *Solid State Ionics*, 2019, **340**, 115019.
45. A. H. Larsen, J. J. Mortensen, J. Blomqvist, I. E. Castelli, R. Christensen, M. Dułak, J. Friis, M. N. Groves, B. Hammer and C. Hargus, *Journal of Physics: Condensed Matter*, 2017, **29**, 273002.
46. J. Enkovaara, C. Rostgaard, J. J. Mortensen, J. Chen, M. Dułak, L. Ferrighi, J. Gavnholt, C. Glinsvad, V. Haikola and H. Hansen, *Journal of physics: Condensed matter*, 2010, **22**, 253202.
47. J. J. Mortensen, L. B. Hansen and K. W. Jacobsen, *Phys. Rev. B*, 2005, **71**, 035109.
48. B. Hammer, L. B. Hansen and J. K. Nørskov, *Phys. Rev. B*, 1999, **59**, 7413.
49. https://nano.ku.dk/english/research/theoretical-electrocatalysis/katladb/au_cu_pd_annealing_in_gases/.
50. M. Friedrich and M. Armbrüster, *Chem. Mater.*, 2009, **21**, 5886-5891.
51. C. Solliard and M. Flueli, *Surface Science*, 1985, **156**, 487-494.
52. M. Fukuhara, *Physics Letters A*, 2003, **313**, 427-430.
53. H. King and F. Manchester, *Journal of Physics F: Metal Physics*, 1978, **8**, 15.
54. T. Barth and G. Lunde, *Z. Phys. Chem.*, 1926, **121**, 78-102.
55. J. Waser, H. A. Levy and S. Peterson, *Acta Crystallographica*, 1953, **6**, 661-663.
56. J. F. Weaver, J. Choi, V. Mehar and C. Wu, *ACS Catalysis*, 2017, **7**, 7319-7331.
57. W. L. Bragg, *The London, Edinburgh, and Dublin Philosophical Magazine and Journal of Science*, 1914, **28**, 355-360.
58. S. Åsbrink and L.-J. Norrby, *Acta Crystallographica Section B: Structural Crystallography and Crystal Chemistry*, 1970, **26**, 8-15.
59. R. Restori and D. Schwarzenbach, *Acta Crystallographica Section B: Structural Science*, 1986, **42**, 201-208.
60. G. K. P. Dathar, W. A. Shelton and Y. Xu, *The journal of physical chemistry letters*, 2012, **3**, 891-895.
61. C.-W. Yi, K. Luo, T. Wei and D. Goodman, *The Journal of Physical Chemistry B*, 2005, **109**, 18535-18540.
62. H. Tsunoyama, H. Sakurai, Y. Negishi and T. Tsukuda, *J. Am. Chem. Soc.*, 2005, **127**, 9374-9375.
63. M. Comotti, C. Della Pina, R. Matarrese and M. Rossi, *Angew. Chem. Int. Ed.*, 2004, **43**, 5812-5815.
64. V. Petkov, Y. Ren, S. Shan, J. Luo and C.-J. Zhong, *Nanoscale*, 2014, **6**, 532-538.
65. B. Hvolbæk, T. V. Janssens, B. S. Clausen, H. Falsig, C. H. Christensen and J. K. Nørskov, *Nano Today*, 2007, **2**, 14-18.
66. M. Yamauchi and T. Tsukuda, *Dalton Transactions*, 2011, **40**, 4842-4845.
67. C. Johansson and J. Linde, *Annalen der Physik*, 1936, **417**, 1-48.
68. C. Wang, D. P. Chen, X. Sang, R. R. Unocic and S. E. Skrabalak, *ACS Nano*, 2016, **10**, 6345-6353.
69. C. Yokokawa, K. Hosokawa and Y. Takegami, *Carbon*, 1966, **4**, 459-465.
70. M. L. Foo, Q. Huang, J. Lynn, W.-L. Lee, T. Klimczuk, I. Hagemann, N. Ong and R. J. Cava, *Journal of Solid State Chemistry*, 2006, **179**, 563-572.
71. Y.-R. Luo and J. Kerr, *CRC Handb. Chem. Phys.*, 2012, **89**, 89.
72. A. Christensen, A. Ruban, P. Stoltze, K. W. Jacobsen, H. L. Skriver, J. K. Nørskov and F. Besenbacher, *Phys. Rev. B*, 1997, **56**, 5822.

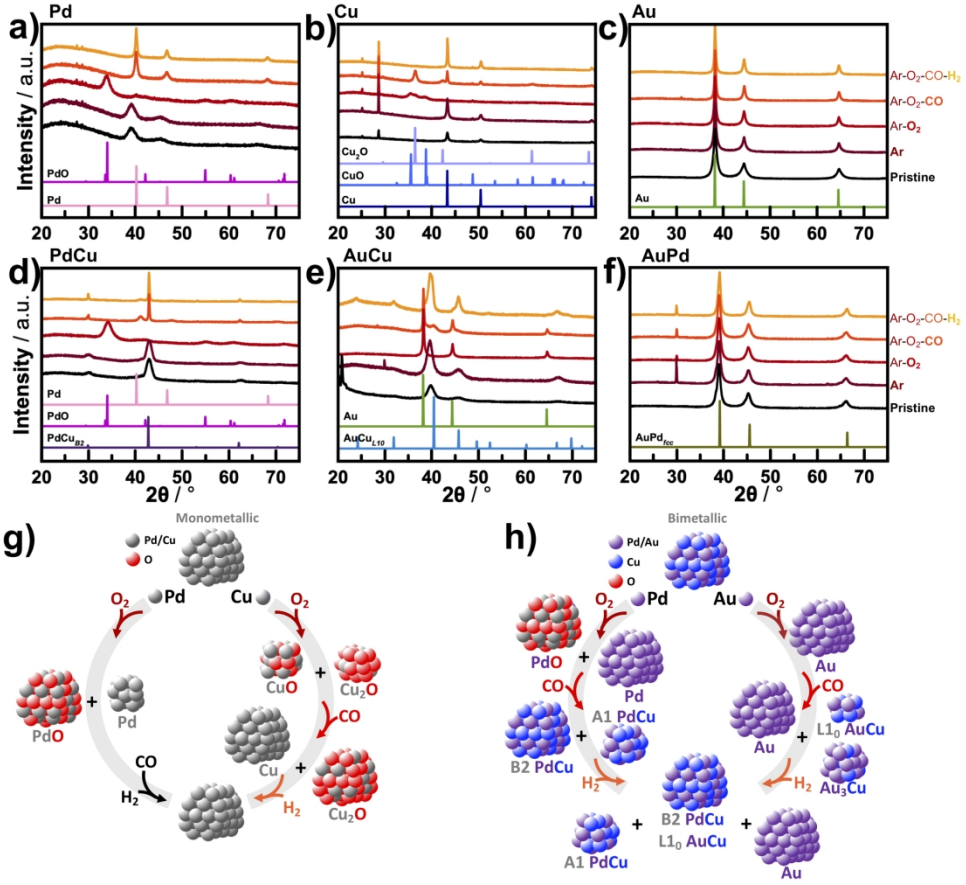

Ex situ PXRD patterns of mono- and bimetallic NCs supported on a glass slide annealed in varying atmospheres. (a-c) show the PXRD patterns and the associated structural changes induced by the gas environment on Pd, Cu and Au NCs, respectively, while (d-f) present the PXRD patterns of PdCu, AuCu and AuPd NCs, respectively. Calculated PXRD patterns of observed structures are shown below the experimental PXRD patterns for each NC system. (g-h) schematically present the observed phase transformations of the mono- and bimetallic NCs, respectively. Note the sharp peaks observed for both (e) Ar-treated AuCu NCs and (f) AuPd at 2θ~30○, which cannot be identified as originating from the binary structures. Instead, these peaks are most likely related to unreacted Au3+ precursor sintering upon heating.

176x161mm (300 x 300 DPI)

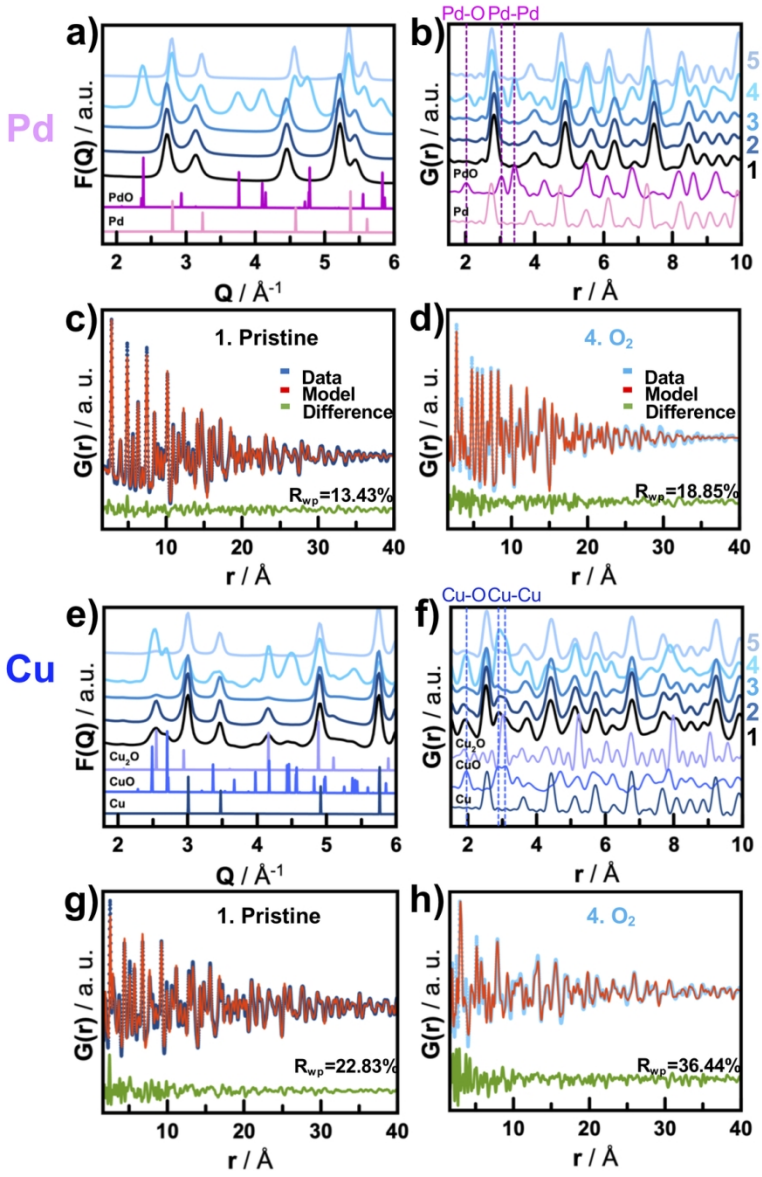

Ex situ X-ray TS data of monometallic NCs supported on disordered carbon, which were annealed in varying atmospheres. The structural changes induced by the gas environments: 1 (pristine state, no gas), 2 (Ar), 3 (Ar-CO), 4 (Ar-CO-O2) and 5 (Ar-CO-O2-H2) are shown in both (a,e) reciprocal space, F(Q), and (b,f) real space, G(r), together with PDF refinements of (c,g) pristine and (d,h) O2-annealed Pd and Cu NCs, respectively.

102x153mm (300 x 300 DPI)

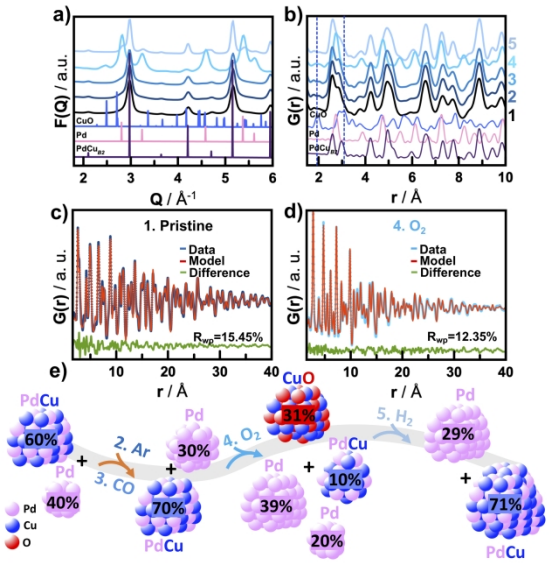

Ex situ X-ray TS data of PdCu NCs supported on disordered carbon, which were annealed in varying atmospheres. The structural changes induced by the gas environments: 1 (pristine state, no gas), 2 (Ar), 3 (Ar-CO), 4 (Ar-CO-O2) and 5 (Ar-CO-O2-H2) are shown in both (a) reciprocal space, F(Q), and (b) real space, G(r). PDF refinements of (c) pristine and (d) O2-annealed NCs. (e) Schematic representation of the observed phase transformations under varying atmospheres.

338x190mm (300 x 300 DPI)

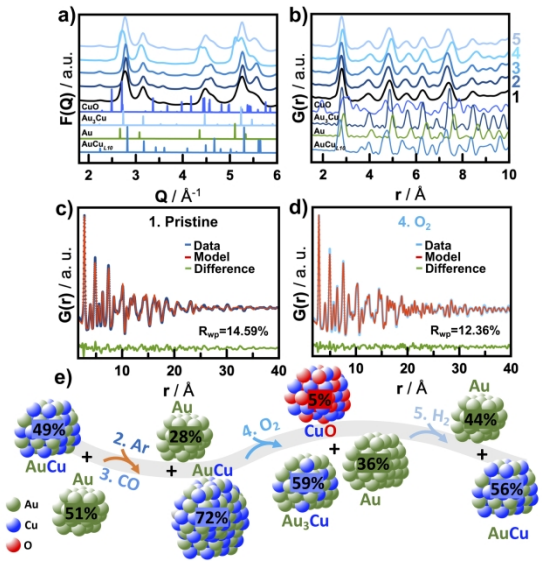

Ex situ X-ray TS data of AuCu NCs supported on disordered carbon, which were annealed in varying atmospheres. The structural changes induced by the gas environments: 1 (pristine state, no gas), 2 (Ar), 3 (Ar-CO), 4 (Ar-CO-O2) and 5 (Ar-CO-O2-H2) are shown in both (a) reciprocal space, F(Q), and (b) real space, G(r). PDF refinements of (c) pristine and (d) O2-annealed NCs. (e) Schematic representation of the observed phase transformations under varying atmospheres.

338x190mm (300 x 300 DPI)

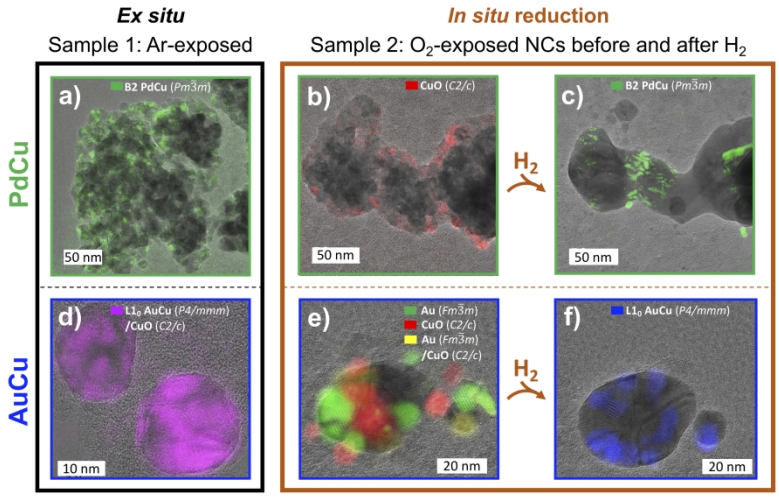

Phase identification with the resulting structural distribution on aggregates of Cu-containing bimetallic NCs on carbon support using HR-TEM imaging. (a) and (d) show the Ar-exposed NCs with B2 PdCu (Pm-3m) and L10 AuCu (P4/mmm) / CuO (C2/c) crystalline structures, respectively, located by the transparent, coloured overlayers as indicated. (b) and (e) display the spatial distribution of crystalline phases (CuO (C2/c)), Au (Fm-3m)) and Au/CuO on the O2-exposed PdCu and AuCu NCs, respectively. (c) and (f) present the O2-exposed PdCu and AuCu NCs, respectively, after being ramped in 1 mbar H2 to 350 ○C at a heating ramp of 1 ○C/min, and reduced in situ at 350 ○C for ca. 5 min within the microscope. Note that both the Ar- and O2-exposed PdCu and AuCu NCs were exposed to air before introduced into the microscope.

338x190mm (300 x 300 DPI)